Supporting Information

Low-temperature pyrolysis enables the $FeNi_3$ nanoparticles implanted N-doped carbon nanosheets as an efficient bifunctional electrocatalyst for overall water splitting

Rong Xin[a], *Yijiang Liu*[a]*, *Xuxin Li*[a], *Shicheng Yi*[a], *Mingyue Zhang*[b], *Hongbiao Chen*[a], *Huaming Li*[a], and *Zhiqun Lin*[b]*

[a] College of Chemistry and Key Laboratory of Environmentally Friendly Chemistry and Application of Ministry of Education, Xiangtan University, Xiangtan 411105, Hunan Province, China

[b] Department of Chemical and Biomolecular Engineering, National University of Singapore, Singapore, 117585

Corresponding Authors

Y.J. Liu (liuyijiang84@xtu.edu.cn); Z.Q. Lin (z.lin@nus.edu.sg)

1. Characterization

Fourier transform infrared spectroscopy (FTIR, Nicolet 6700 spectrophotometer) and powder X-ray diffraction (XRD, Rigaku D/Max 2500PC diffractometer) were employed to characterize the chemical compositions and crystal structures of as-prepared samples. Furthermore, filed-emission scanning electron microscope (SEM, JEOL S-4800) and transmission electron microscope (TEM, JEOL JEM-1011) were utilized to distinguish the shape of the as-prepared samples. The samples were

dropped on the silica plate and air-dried, and then observed at an accelerating voltage of 10 kV. The samples were dipped on the copper grids and air-dried, and the morphology was visualized by using TEM at an accelerating voltage of 100 kV. High-resolution transmission electron microscope (HRTEM) and elemental mapping analysis were measured by JEOL JEM-2100. The morphology of the samples was imaged by The X-ray photoelectron spectroscopy (XPS) was measured on a K-Alpha 1063 photoelectron spectrometer (Thermo Fisher Scientific, England) using Al-Kα X-ray radiation as an excitation source. The porosity was characterized by nitrogen adsorption experiments at 77.3 K (Micromeritics Tri Star II 3020). Brunauer-Emmett-Teller (BET) method was used to calculate the specific surface area. The pore size distribution (PSD) was calculated from the adsorption branches of the isotherms using the DFT model.

2. Electrochemical measurements

The HER and OER performance was tested in 1.0 M KOH solution with the three-electrode system using CHI760D electrochemical workstation at room temperature. The Carbon paper supported active materials with a geometric area of 0.5×0.5cm was immersed into the solution as the working electrode. The loading mass of $FeNi_3$/NCS on the carbon paper is 1.0 mg cm^{-2}. A standard Hg/HgO electrode and graphite rod were served as the reference and counter electrodes, respectively. Notably, the mass loading of RuO_2 and 20 wt %Pt/C catalysts on the carbon paper is also 1.0 mg cm^{-2}.

The working electrode was fabricated as follows: the catalyst ink was prepared by dispersing 4.0 mg of $FeNi_3$/NCS or 20 wt % Pt/C or RuO_2 in a mixed solvents of deionized water (785 μL), ethanol (200 μL) and 5% nafion (15 μL) under ultrasonication. Subsequently, 64 μL of the catalyst ink was drop-cast onto a piece of clean carbon paper (0.5 cm × 0.5 cm), and the prepared electrode was dried under infrared light before electrochemical measurements.

Before OER and HER activity test, 1.0 M KOH electrolyte was saturated with O_2 and N_2 for at least 30 min to ensure the O_2 saturation and mitigate dissolved oxygen.

Prior to LSV test, the working electrode was pre-activated by 20 cycles of cyclic voltammetry (CV) scan. The potential ranges are from 0 V to 1.0 V for OER and from -1.8 V to 0 V for HER, respectively. The electrochemical impedance spectrum (EIS) test of the catalysts were carried out with a frequency range of 1 Hz to 10 kHz at the overpotential corresponding to the current density of 10 mA cm^{-2}. To evaluate the activity of the obtain samples, the linear sweep voltammetry (LSV) was performed between 0 V to 1.0 V for OER, -0.8V to -1.5 V for HER at 5 mV s^{-1}, respectively. All the LSV tests were performed with 80% iR compensation. The electrochemical surface area (ESCA) was estimated from the double-layer capacitance (C_{dl}) of the electrocatalyst materials. The C_{dl} was determined by a simple CV method. The CV was conducted at various scan rates of 20, 40, 60, 80 and 100 mV s^{-1}. The stability of the catalyst was proved by chronopotentiometry.

TOF is another intrinsic activity parameter that could be derived from that current density at a fixed potential and the surface concentration or number of actually involved metal sites. However, getting an accurate TOF is always a difficult task unless the catalyst under study is a single-crystal electrocatalyst of well-faceted planes or a molecular electrocatalyst as several assumptions have to be made. To prove this, we have calculated the TOFs using the following equation:

$$TOF = j \cdot N_A / n \cdot F \cdot \Gamma$$

where j is the current density, N_A is the Avogadro number, n is the number of electron transferred for the evolution of a single O_2 molecule, F is the Faraday constant (96485 $C \cdot mol^{-1}$) , and Γ is the surface concentration or the number of active sites.

Overall water splitting performance tests were performed using CHI760D electrochemical workstation with the $FeNi_3$/NCS as both the cathode and anode catalyst. LSV measurement was carried out in 1.0 M KOH solution with a scan rate of 5 mV s^{-1}. The overall waters plitting stability of the obtained samples was measured by chronoamperometry for 12 h at a constant potential of 1.53 V corresponding to the current density of 10 mA cm^{-2}.

All measured potentials in this study were converted to RHE according to the following equation:

$$E_{RHE} = E_{Hg/HgO} + 0.098 + 0.0591pH$$

In overall water splitting, Faraday efficiency is calculated by the following equation:

$$FE\% = V_{experimental} / V_{theoretical}$$

The actual volume of H_2 and O_2 produced can be calculated by the drainage method, the theoretical volume of H_2 and O_2 produced can be calculated by the following equation:

$$V_{theoretical} = I \times t \times V_m / n \times F$$

where I (A) is the current of overall water splitting, t (s) is spent time of overall water splitting, V_m is the molar volume of gas at normal temperature and pressure (24.5 L mol^{-1}, 298K, 101 kPa), n is the number of electrons required to electrolyze 1 mole gas (O_2 : n=4; N_2 : n=2), F is the faraday constant (96485 C mol^{-1}).

3. DFT Calculation

3.1 Construction of model

The $FeNi_3$ crystal structure has a space group of PM-3M with cell parameters of $\alpha = \beta = \gamma = 90°$, a = b = c = 3.51 Å,and the (111) plane was selected as the reaction crystal plane. We constructed a (5×5) $FeNi_3$ (111) model with cell parameters a = b = 9.92 Å, c = 21.2 Å to calculate the catalysis ability. The supercell graphite structure was used with the random N-doping model where the lattice parameters, a = b = 9.85 Å and c = 16 Å. In addition, we replaced some carbon atoms in the supercell graphite model by Ni and Fe atoms (Ni:Fe=3:1) to construct $FeNi_3$ slab model. All the models were geometrically optimized, and the top two layers were allowed to relax.

3.2 Computational methods

All the calculations are performed in the framework of the density functional theory with the projector augmented plane-wave method, as implemented in the Vienna ab initio simulation package. The generalized gradient approximation proposed by Perdew, Burke, and Ernzerhof is selected for the exchange-correlation

potential. The cut-off energy for plane wave is set to 520 eV. The energy criterion is set to 10^{-5} eV in iterative solution of the Kohn-Sham equation. Spin-polarized calculations are adopted to explore the magnetic states of bulk structures. The Brillouin zone was sampled with allowed spacing between k points in 0.1 $Å^{-1}$, with Γ-centered Monkhorst−Pack k-point grid. For the slab model calculations, the vacuum distance was carefully tested and set to be 12 Å to avoid the cell-to-cell interactions. All the structures are relaxed until the residual forces on the atoms have declined to less than 0.01 eV/Å. The visualization of three-dimensional structures is employed by VESTA software.

The OER performance of the catalysts was assessed by the adsorption free energy change (ΔG_{rds}) of the intermediates by the following four-step elementary reactions in alkaline conductions.

$$OH^- + * \rightarrow OH^* + e^-$$

$$OH^* + OH^- \rightarrow O^* + H_2O + e^-$$

$$O^* + OH^- \rightarrow OOH^* + e^-$$

$$OOH^* + OH^- \rightarrow * + O_2 + H_2O + e^-$$

The Gibbs free energies of ΔG_{OH^*}, ΔG_{O^*}, ΔG_{OOH^*} are defined based on the OH*, O*, OOH* absorption on the electrocatalyst models, which are calculated according to the following equation:

$$\Delta G_{ads} = \Delta E_{ads} + \Delta E_{ZPE} - T\Delta S_{ads} - eU - kT\ln 10 \times pH$$

Where ΔE_{ads} is the absorption energy, ΔE_{ZPE} is the zero point energy calculated from the vibration frequency, ΔS_{ads} is the entropy change, k is the boltzmann constant, T is the reaction temperature (300K), U represents the external bias voltage and pH is referred to as acidity. Here, for the standard alkaline conditions, pH=14, U=0.

The overpotential η for OER reaction at a particular active site can be evaluated as the difference between ΔG and the equilibrium potential (U=1.23 V):

$$\eta_{OER} = \max[\Delta G_1, \Delta G_2, \Delta G_3, \Delta G_4]/e - 1.23\text{V}$$

Similarly, the three steps of hydrogen evolution reaction (HER) process under alkaline conditions are considered to explore the electrocatalyst properties of

$FeNi_3$/NCS, $FeNi_3$ and NCS.

$$H_2O + *+ e^- \rightarrow OH^- + H*$$

$$H* + H_2O + e^- \rightarrow OH^- + H_2$$

$$H* + H* \rightarrow H_2$$

The differential charge density of $FeNi_3$/NCS is defined by

$$\Delta\rho\ (FeNi_3/NCS) = \rho\ (FeNi_3/NCS) - \rho\ (NCS)$$

where the $\rho\ (FeNi_3/NCS)$, $\rho\ (NCS)$ is the charge density of $FeNi_3$/NCS, NCS, respectively.

4. Figures

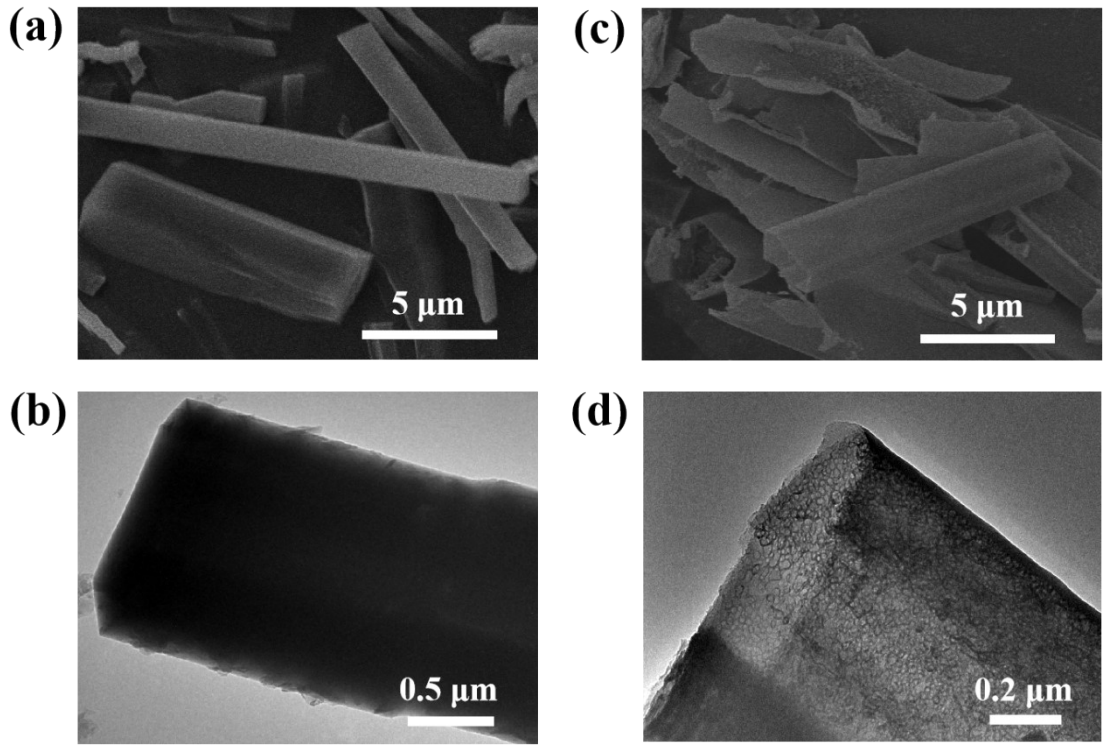

Fig. S1. SEM and TEM images of (a, b) Mel-T, (c, d) NCT.

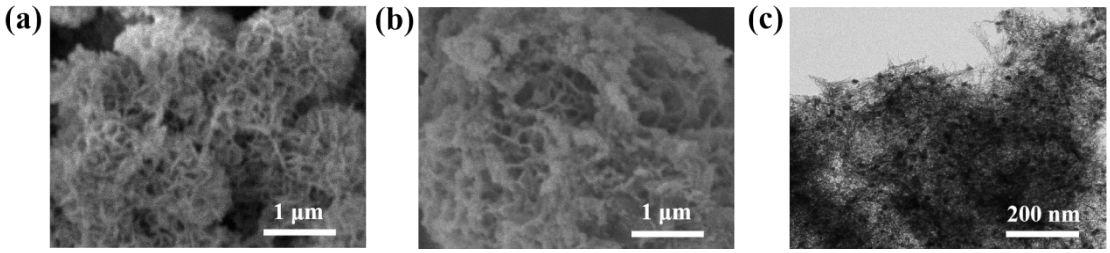

Fig. S2. (a) SEM of FeNi-LDH, and SEM (b) and TEM images (c) FeNiO/C.

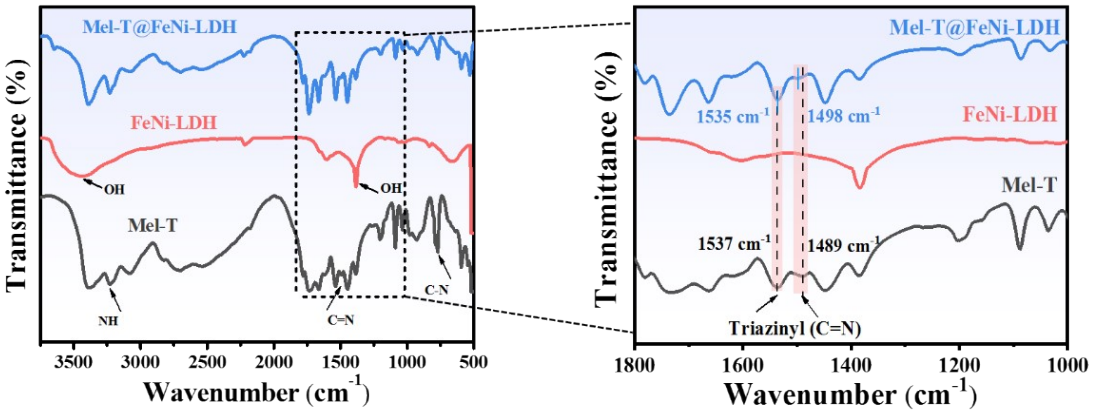

Fig. S3. The FTIR spectra of Mel-T, FeNi-LDH and Mel-T@FeNi-LDH.

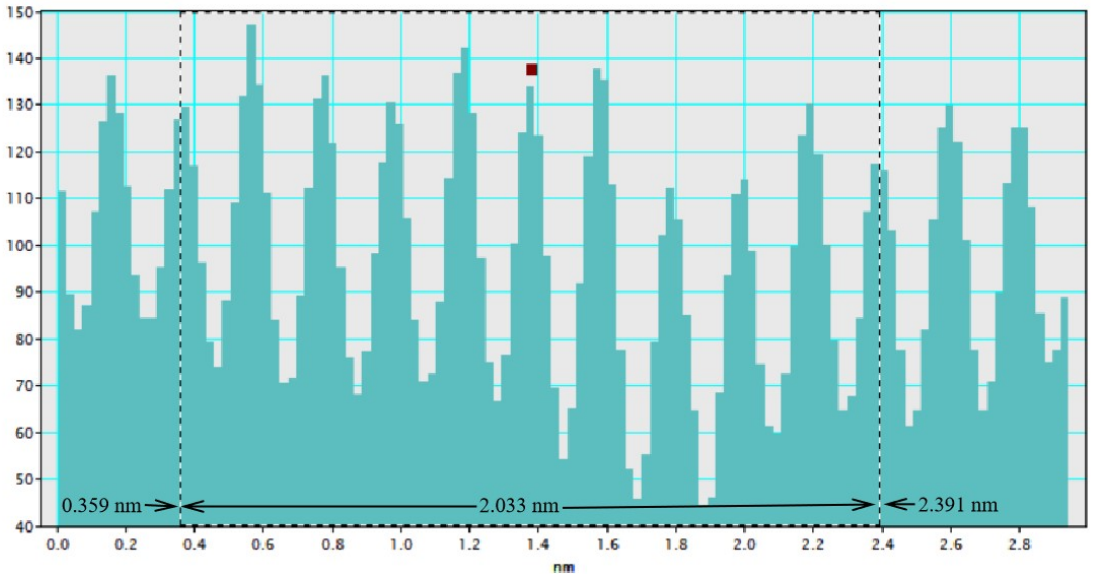

Fig. S4. The average lattice spacing of $FeNi_3$ (111) in the $FeNi_3$/ NCS electrocatalyst.

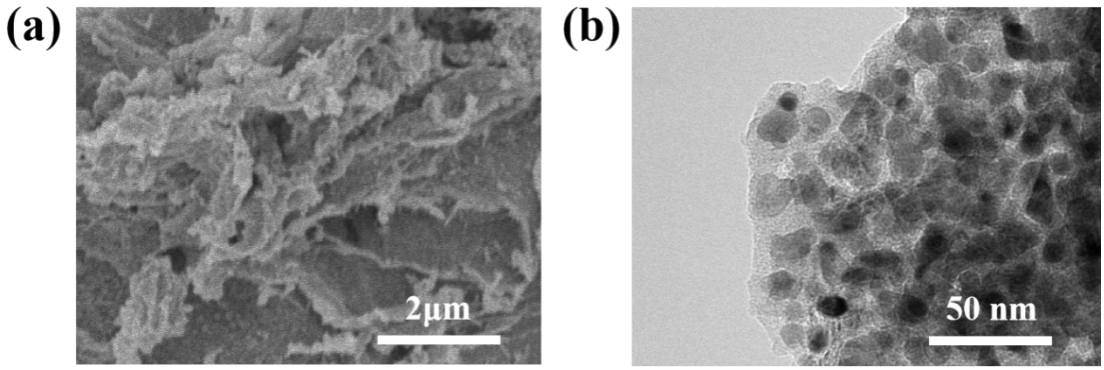

Fig. S5. SEM and TEM images of FeNi/NC.

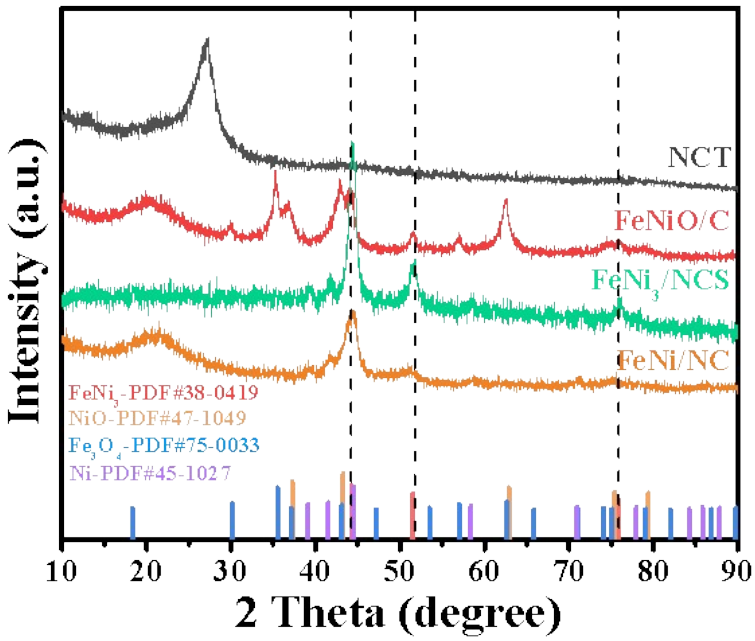

Fig. S6. XRD pattern of NCT, FeNiO/C, $FeNi_3$/NCS, FeNi/NC.

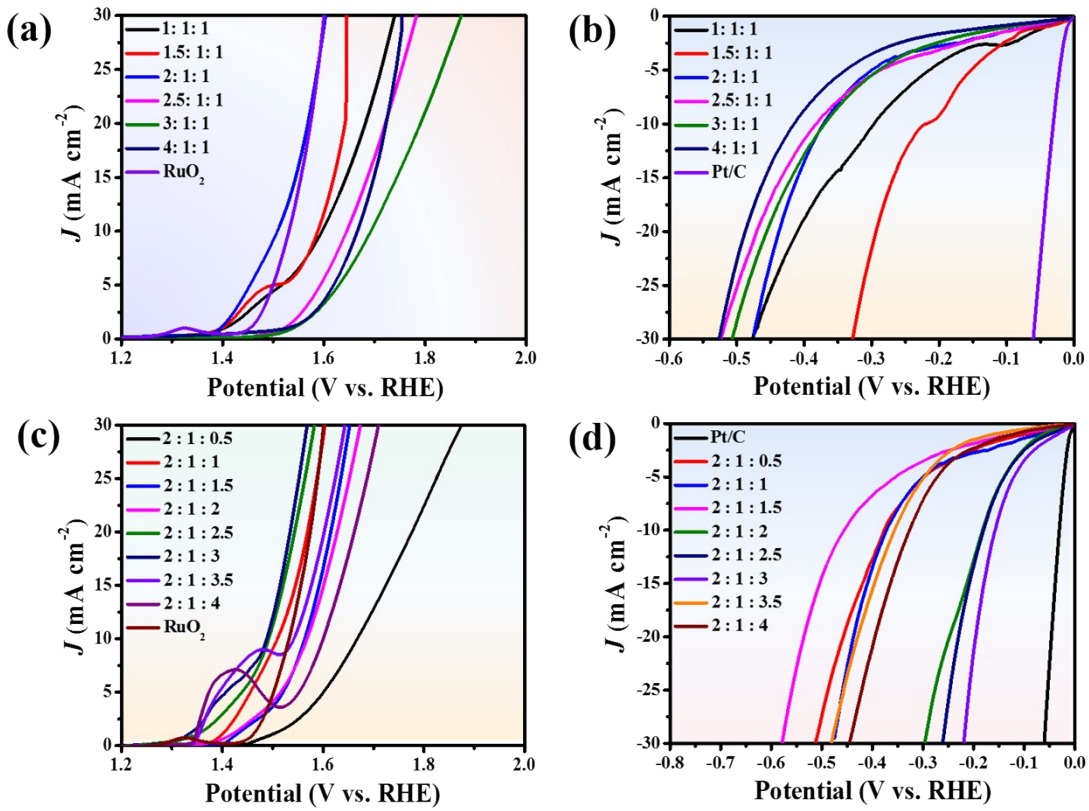

Fig. S7. (a) OER and (b) HER polarization curves of pyrolyzed Mel-T@FeNi-LDH with different mass ratios of melamine tube and metal salts; (c) OER and (d) HER polarization curves of pyrolyzed Mel-T@FeNi-LDH with different mass ratios of Fe^{3+} and Ni^{2+}.

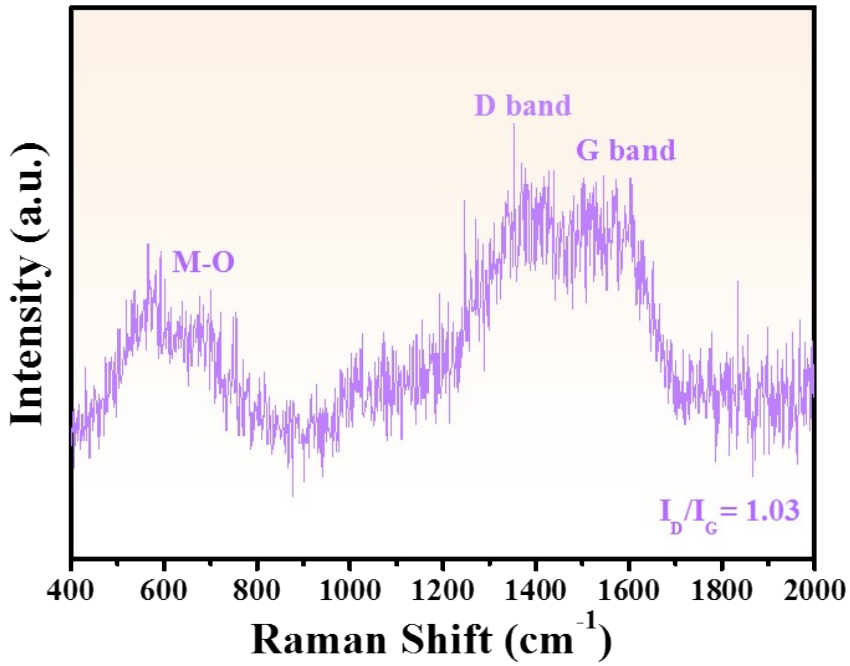

Fig. S8. Raman spectrum of $FeNi_3$/NCS.

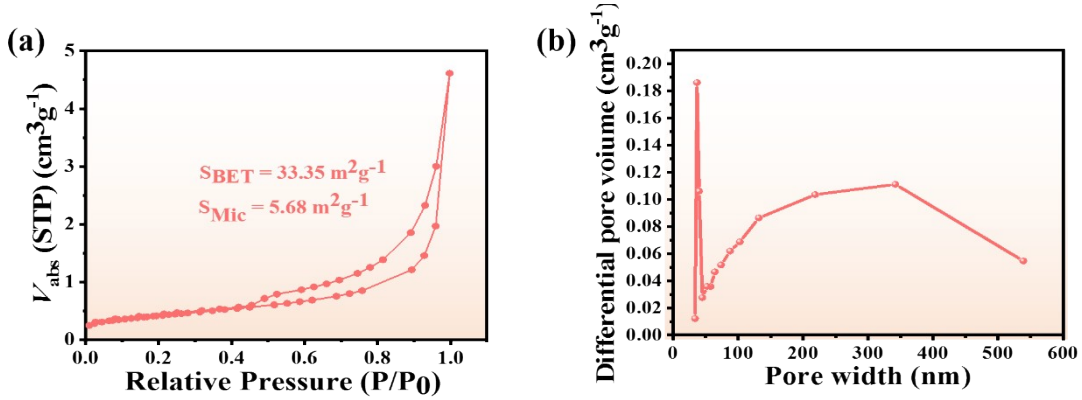

Fig. S9. (a) N_2 adsorption-desorption isotherms, and (b) pore size distribution of $FeNi_3$/NCS.

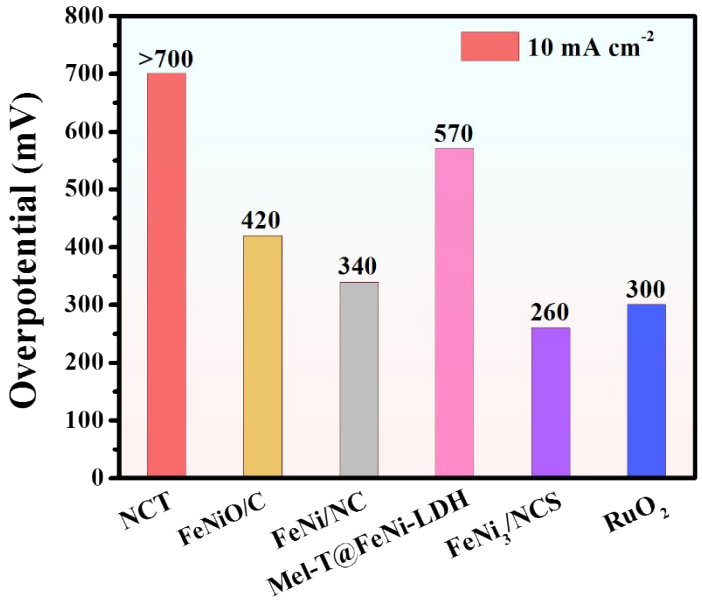

Fig. S10. OER overpotential at 10 mA cm^{-2} of as-prepared samples.

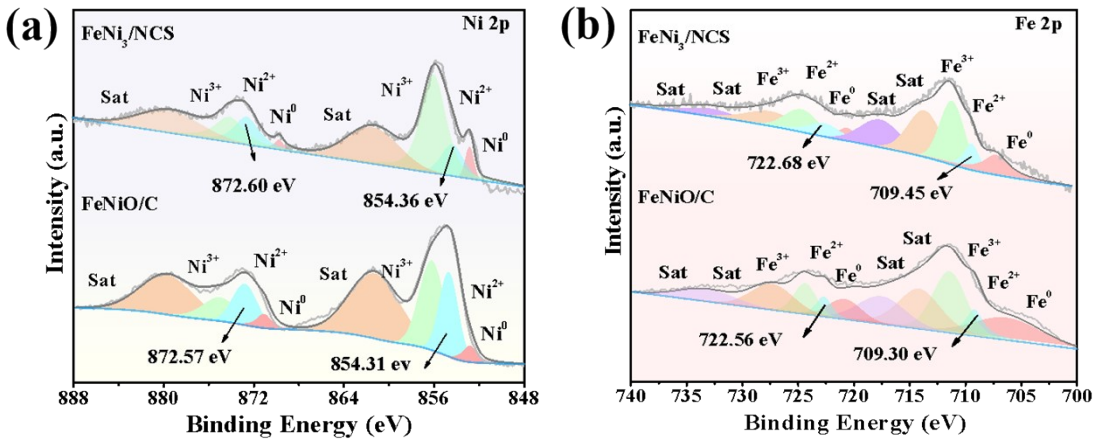

Fig. S11. High-resolution XPS spectra of (a) Ni 2p and (b) Fe 2p in $FeNi_3$/NCS, FeNiO/C.

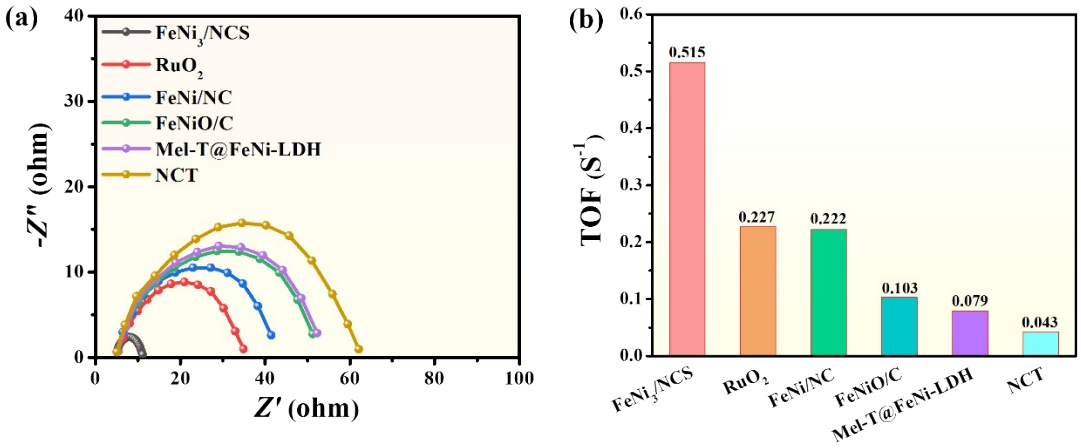

Fig. S12. (a) Nyquist plots, (b) TOF of $FeNi_3$/NCS, NCT, FeNiO/C, FeNi/NC, Mel-T@FeNi-LDH and RuO_2 at 1.60 V.

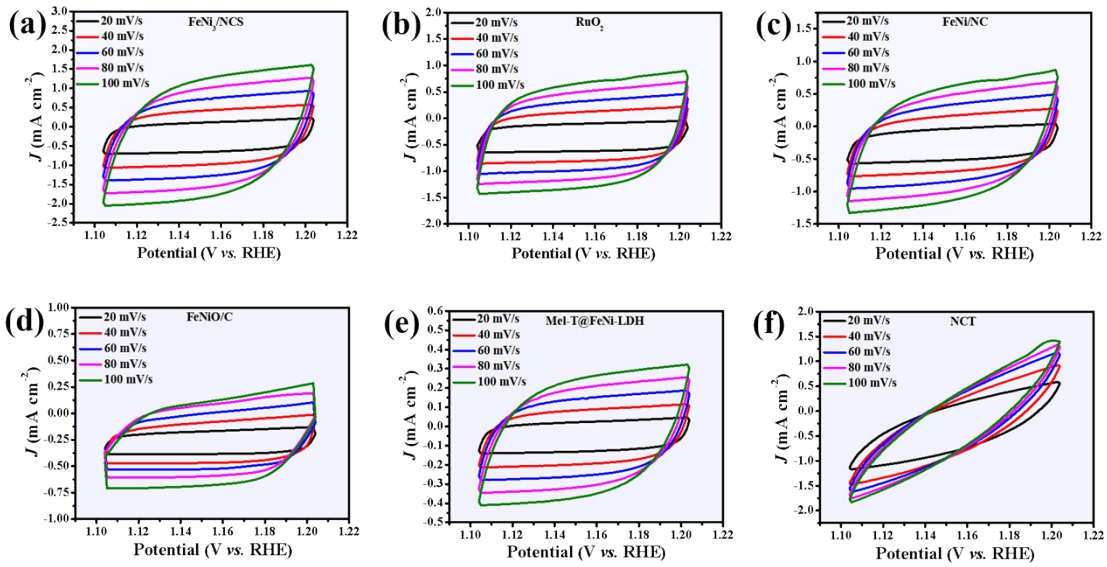

Fig. S13. Cyclic voltammetry (CV) curves of NCT, FeNiO/C, $FeNi_3$/NCS, FeNi/NC, Mel-T@FeN-LDH and RuO_2 in O_2-saturated 1.0 M KOH solution at different scan rates.

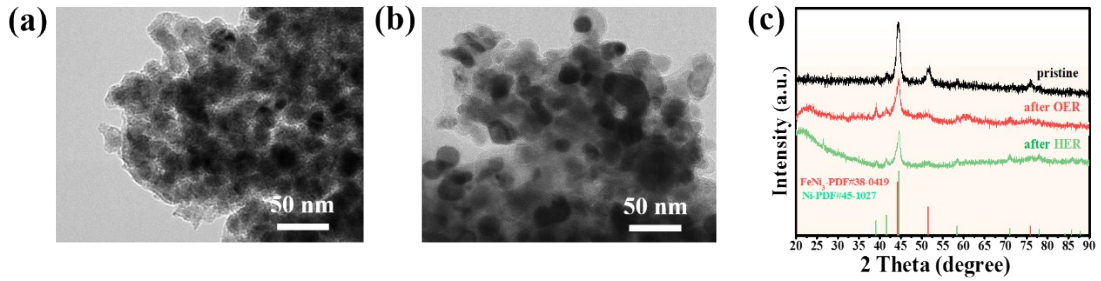

Fig. S14. TEM images of $FeNi_3$/NCS after stability tests: (a) OER and (b) HER, and (c) XRD patterns after OER and HER stability testing.

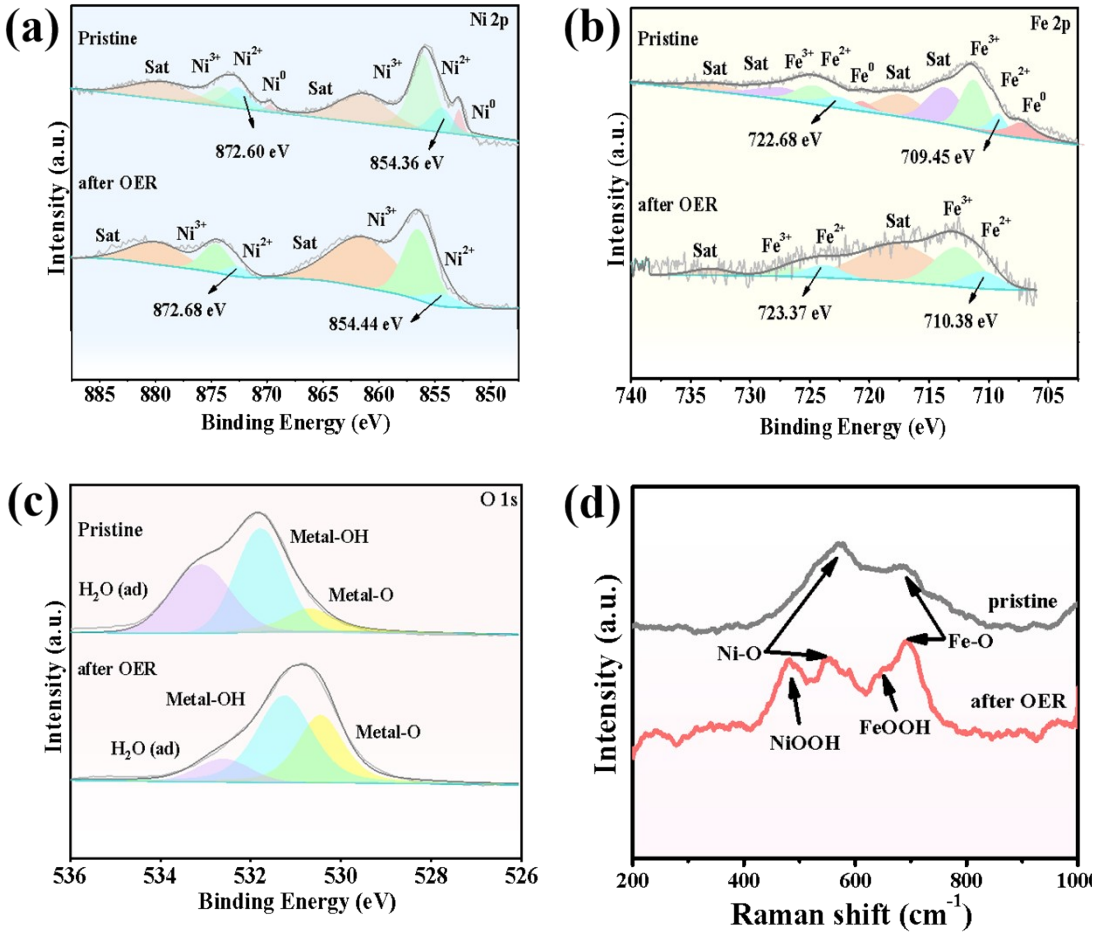

Fig. S15. High-resolution XPS spectra of (a) Ni 2p, (b) Fe 2p, (c) O 1s of $FeNi_3$/NCS before and after OER stability test; (d) Raman spectrum of $FeNi_3$/NCS before and after OER stability test.

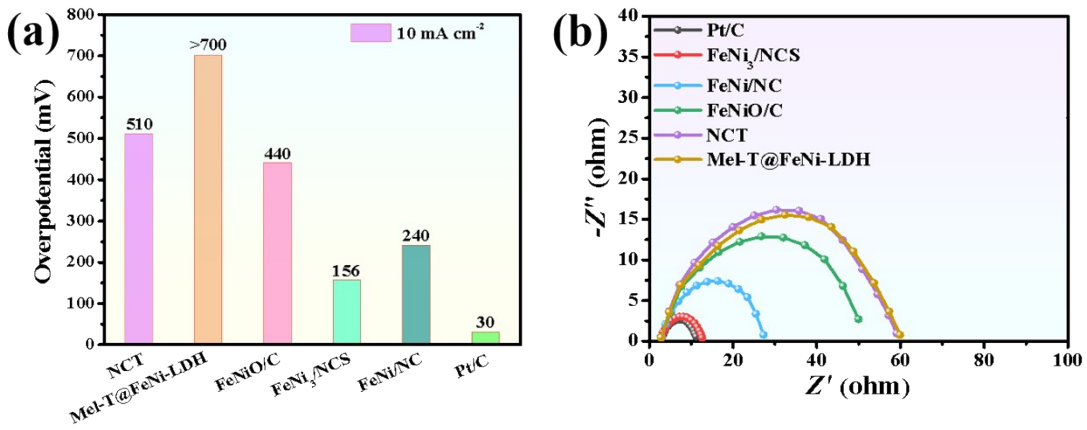

Fig. S16. (a) Overpotential at 10 mA cm^{-2} of the as-prepared samples, (b) Nyquist plots of NCT, FeNiO/C, FeNi/NC, Mel-T@FeNi-LDH, $FeNi_3$/NCS, and Pt/C.

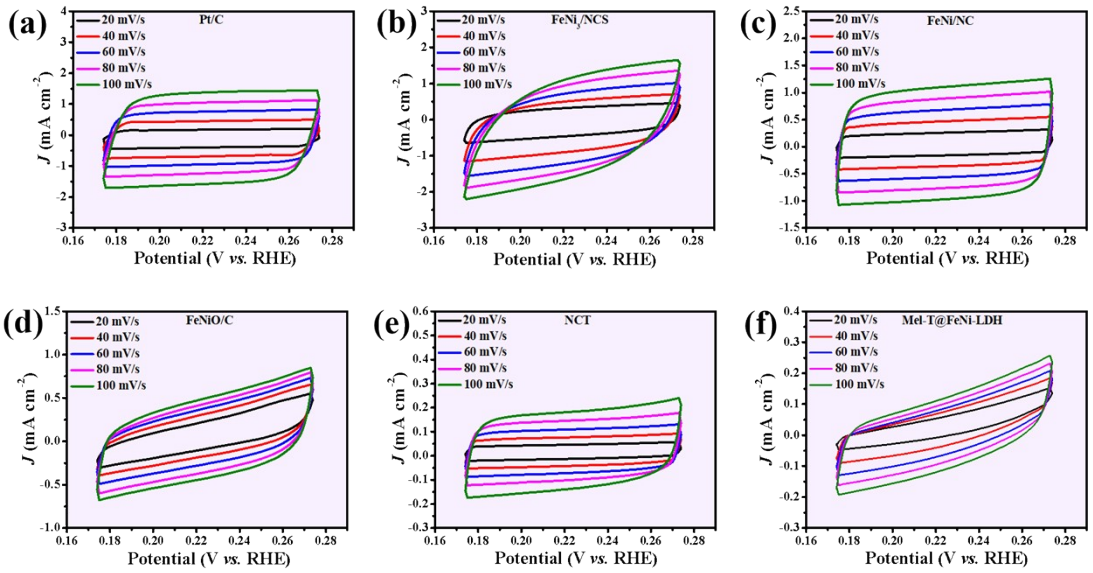

Fig. S17. Cyclic voltammetry (CV) curves of NCT, FeNiO/C, $FeNi_3$/NCS, FeNi/NC, Mel-T@FeN-LDH and Pt/C in N_2-saturated 1.0 M KOH solution at different scan rates.

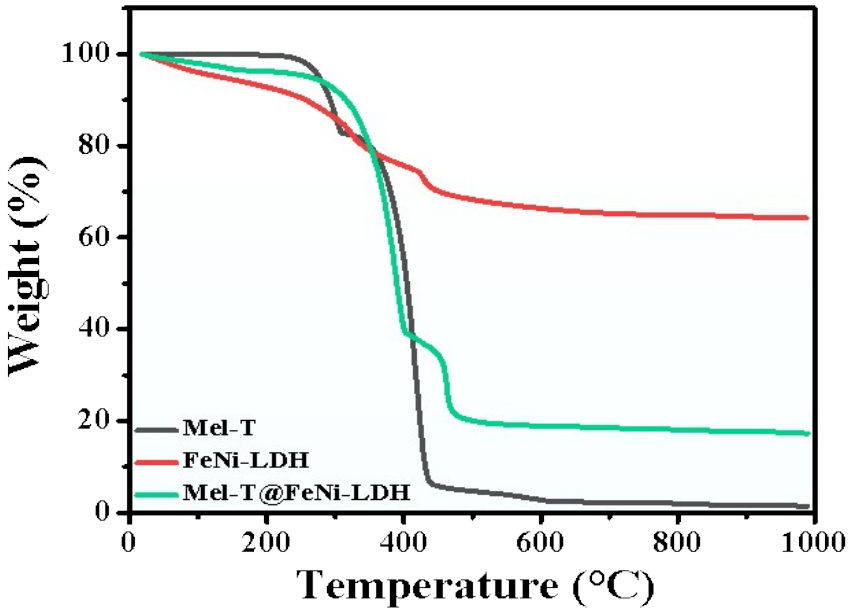

Fig. S18. TG curves of Mel-T, FeNi-LDH and Mel-T@FeNi-LDH.

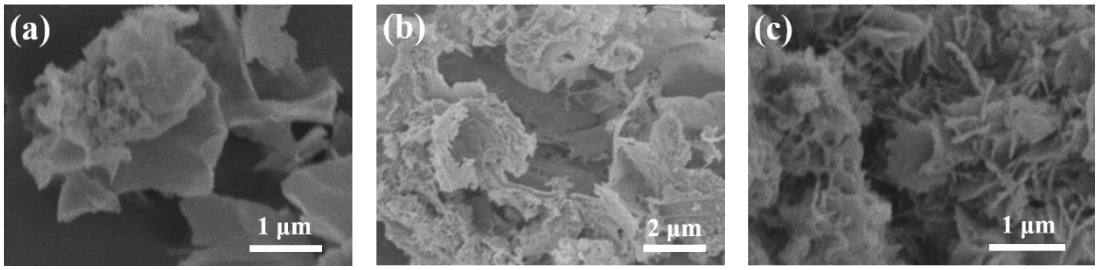

Fig. S19. SEM images of Mel-T@FeNi-LDH after pyrolysis at (a) 350 °C; (b) 400 °C h; and (c) 450 °C.

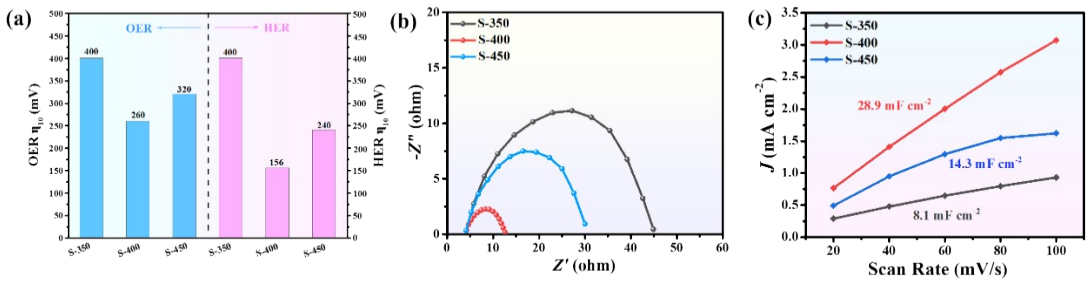

Fig. S20. (a) Overpotentials of HER and OER at different pyrolysis temperatures, (b) Nyquist plots, (c) C_{dl} of the carbonized samples.

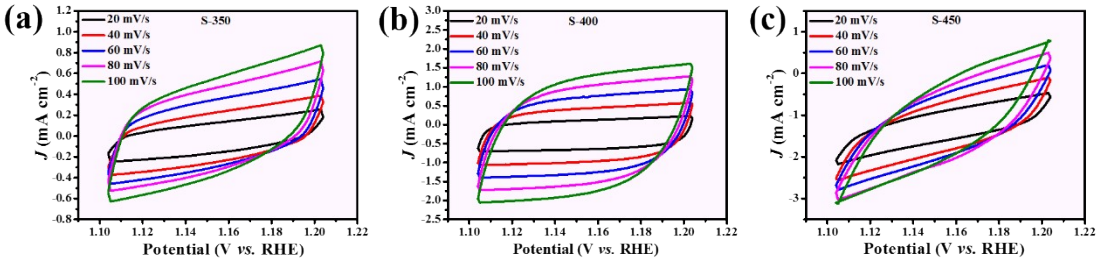

Fig. S21. Cyclic voltammetry (CV) curves of S-350, S-400 and S-450 in O_2-saturated 1.0 M KOH solution at different scan rates.

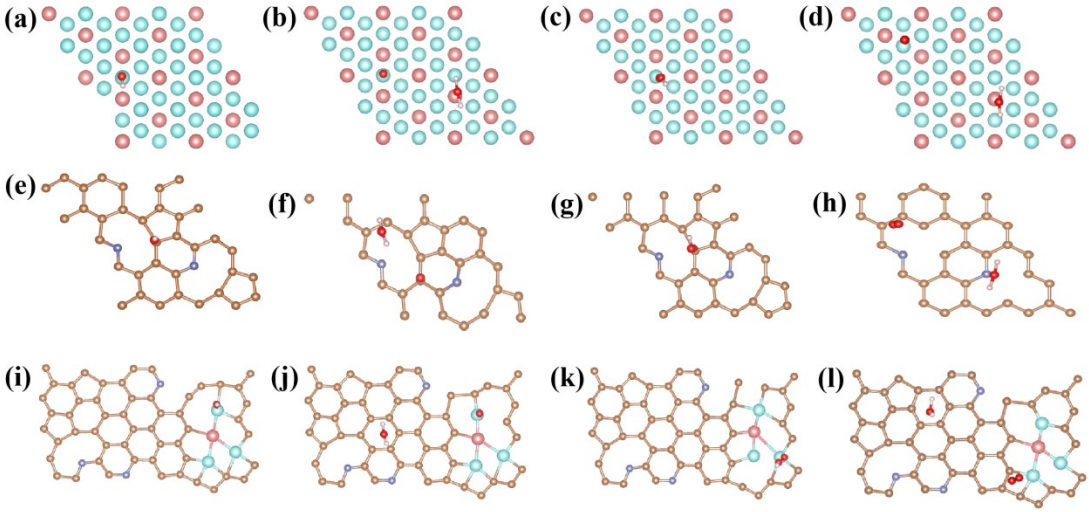

Fig. S22. The structure models of $FeNi_3$, NCS and $FeNi_3$/NCS after adsorbing (a) (e) (i) OH*; (b) (f) (j) O*; (c) (g) (k) OOH*; (d) (h) (l) release of oxygen. Silver, green, pink, brown, blue, red and light pink balls indicate Ni, Fe, C, N, O and H atoms, respectively.

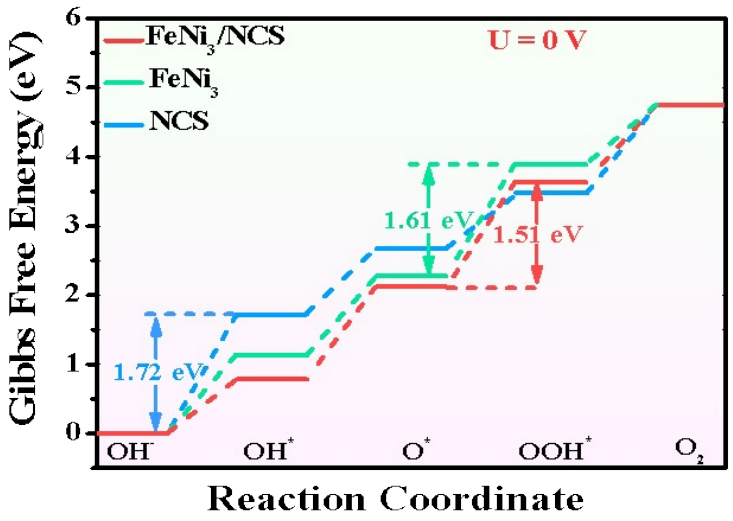

Fig. S23. The Gibbs free energy diagrams of NCS, $FeNi_3$ and $FeNi_3$/NCS towards OER at U = 0 V.

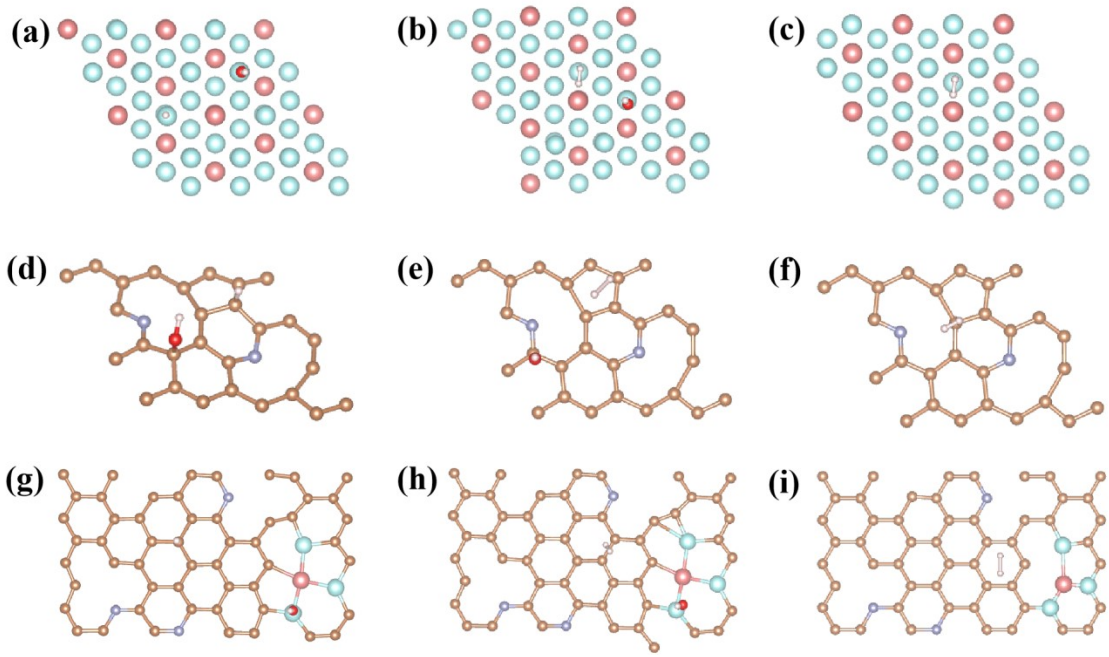

Fig. S24. (a) (d) (g) The structure models of $FeNi_3$, NCS and $FeNi_3$/NCS with Volmer reaction; (b) (c) (h) The structure models of $FeNi_3$, NCS and $FeNi_3$/NCS with Heyrovsky reaction; (c) (f) (i) The structure models of $FeNi_3$, NCS and $FeNi_3$/NCS with Tafel reaction.

5. Tables

Table S1. Comparison of OER performance of previous studies with this work in 1.0 M KOH solution.

Catalyst	η_{10} (mV)	*J* (mA cm^{-2})	References
Ni_1Co_1-LDHs-E_1D_1	260	10	*Sustainable Mater. Technol.* 2020, 25, e00170
Ni_3Fe/rGO	280	10	*Chem. Eng. J.* 2022, 451, 138548
NiFe-LDH NSs	280	10	*ACS Appl. Energy Mater.* 2019, 2, 5465-5471
CoMoV LDH/NF	270	10	*Chem. Comm.* 2019, 55, 3521-3524
Ni_3N-NiMoN	277	10	*Nano Energy* 2018, 44, 353-363
Co/CNT/MCP	270	10	*Carbon* 2020, 166, 284-290
CoP-NC@NFP	270	10	*Chem. Eng. J.* 2022, 428, 131115
H-CoSx@NiFe LDH/NF	250	10	*Small* 2022, 2200586
MoS_2/NiFe LDH	257	10	*Chinese Chem. Lett.* 2022, 33, 4761-4765
Fe-Co-CN/rGO-700	308	10	*Electrochim. Acta* 2021, 365, 137384
Ni/NiS/NC	337	10	*Int. J. Hydrogen Energy* 2019, 44, 2832
Ni-Mo_xC/NC	328	10	*ACS Appl. Mater. Interfaces* 2018, 10, 35025
CoFe-LDH	267	10	*ACS Appl. Energy Mater.* 2022, 5, 11483
$FeNi_3$/NCS	**260**	**10**	**This work**

Table S2. Comparison of HER performance of previous studies with this work in 1.0 M KOH solution.

Catalyst	η_{10} (mV)	J (mA cm^{-2})	References
CoFe@NiFe/NF	240	10	*Appl. Catal. B.* 2019, 253, 131-139
Ni_3Fe/rGO	264	10	*Chem. Eng. J.* 2022, 451, 138548
NiFe LDH/(NiFe)S_x/CMT	157	10	*Electrochim. Acta* 2020 , 348, 136339
CoMoV LDH/NF	150	10	*Chem. Comm.* 2019, 55, 3521-3524
Cr-doped FeNi-P/NCN	190	10	*Adv. Mater.* 2019, 31, 1900178
RuO_2-Fe_2O_3/HrGO NSs	239	10	*Int. J. Hydrogen Energ,* 2022,
CoP-NC@NFP	162	10	*Chem. Eng. J.* 2022, 428, 131115
Fe-Co-CN/rGO-700	215	10	*Electrochim. Acta* 2021, 365, 137384
Ni_3S_2/Cu-NiCo LDH/NF	156	10	*J. Mater. Chem. A* 2021, 9, 27639-27650
Ni-Mo_xC/NC	162	10	*ACS Appl. Mater. Interfaces* 2018, 10, 35025
Ni-NiO@3DHPG	310	10	*Electrochim. Acta* 2019, 298, 163
Fe_3C-Co/NC	238	10	*Adv. Funct. Mater.* 2019, 29, 1901949
$FeNi_3$/NCS	**156**	**10**	**This work**

Table S3. Comparison of overall water splitting performance with of previous studies and this work in 1.0 M KOH solution.

Catalyst	Cell voltage	Current density (mA cm^{-2})	References
CoFe@NiFe/NF	1.59	10	*Appl. Catal. B.* 2019, 253, 131-139
$Ir/Ni_3Fe/rGO$	1.57	10	*Chem. Eng. J.* 2022, 451, 138548
CoMoV LDH/NF	1.61	10	*Chem. Comm.* 2019, 55, 3521-3524
$Pd/NiFeO_x$	1.57	10	*Adv. Funct. Mater.* 2021, 31, 21071-21081
$CoSe_2$@CoNi-LDH HNA	1.58	10	*Adv. Sci.* 2022, 9, 2104522
MoS_2/NiFe LDH	1.61	10	*Chinese Chem. Lett.* 2022, 33, 4761-4765
CoP-NC@NFP	1.57	10	*Chem. Eng. J.* 2022, 428, 131115
H-CoS_x@NiFe LDH/NF	1.59	10	*Small* 2022, 2200586
NiCoFe LDH/NF	1.56	10	*Chem. Eng. J.* 2022, 433 134552
Ni_3S_2/Cu-NiCo LDH/NF	1.58	10	*J. Mater. Chem. A*, 2021, 9, 27639-27650
Cr-doped FeNi-P/NCN	1.50	10	*Adv. Mater.*, 2019, 31, 1900178
CoFeNi-LDH	1.56	10	*J. Power Sources*, 2022, 524, 231068
Ni@NiFe LDH	1.53	10	*J. Mater. Chem. A*, 2019, 7, 21722
NiFe-MOF	1.57	10	*Inorg. Chem. Front*. 2021, 8, 2889
U−Fe-β-$Ni(OH)_2$/NF	1.58	10	*ACS Appl. Mater. Interfaces* 2020, 12, 36208
$FeNi_3$/NCS	**1.53**	**10**	**This work**

Table S4. Gibbs free energy change (G) of NCS, $FeNi_3$, and $FeNi_3$/ NCS at different potential during OER.

ΔG (eV)	**U = 0 V**			**U = 1.23 V**		
	NCS	$FeNi_3$	$FeNi_3$/NCS	NCS	$FeNi_3$	$FeNi_3$/NCS
Step 1	1.7223	1.1292	0.7851	0.4923	-0.1008	-0.4449
Step 2	0.9529	1.1493	1.3401	-0.2771	-0.0807	0.1101
Step 3	0.8071	1.6109	1.5064	-0.4229	0.3809	0.2764
Step 4	1.269	0.8619	1.1197	0.039	-0.3681	-0.1103